The Surface Wave Effects on the Performance and the Loading of a Tidal Turbine

Xiaoxian Guo[a,b], Jianmin Yang[a,b,*], Zhen Gao[c], Torgeir Moan[c], Haining Lu[a,b]

[a] *State Key Laboratory of Ocean Engineering, Shanghai Jiao Tong University, China*
[b] *Collaborative Innovation Center for Advanced Ship and Deep-Sea Exploration, China*
[c] *Department of Marine Technology, Norwegian University of Science and Technology, Norway*

Abstract

When tidal turbines are utilized in the most energetic waters where there are significant waves, the assessment of the surface wave effects are of great concerns. The objective of this paper is to contribute to a fundamental understanding of surface wave effects on tidal turbines. A numerical model was developed based on the modified Blade Element Momentum theory with an inclusion of added mass effects, wave excitation forces and a one degree-of-freedom (DOF) simulation for turbine rotational motion. The experiments on a 1:25 scaled tidal turbine were performed in a towing tank. It is shown that the surface waves did not affect the average loads and power output, but caused severe periodical oscillations. The amplitudes of the cyclic thrust and torque could reach up to 50% of the mean value induced by the incident waves with period of 1.6 s and height of 14 cm. Non-dimensional response amplitude operators (RAOs) of thrust and torque were proved to be sensitive to submergence of the turbine. The wave induced torque and thrust tend to a fixed value when the incident wave length is much longer than the water depth, which provides an approximate assessment of the surface wave effects on tidal turbines.

Keywords: Tidal turbine, Wave loads, Blade Element Momentum, Towing experiments, Regular waves

---

*Corresponding author, Tel: +86 21 34207050, Fax:+86 21 34207058.
Email address: jmyang@sjtu.edu.cn (Jianmin Yang)

1. Introduction

The concept of extracting power from ocean tides has a long history (Elghali et al., 2007) With the growing worldwide energy demand, utilizing tidal turbines to generate power has gained increased attention. Tidal current power has advantages of a high predictability. a high energy density, and limited environmental impacts (Khan et al., 2009; Rourke et al., 2010; Adcock et al., 2015). In many parts of the world, tidal power presents an advantageous resource. About 61.3 TWh/year of tidal current energy technically available in China. Some excellent channels in the East China Sea are most promising sites with the maximum flow speed over 4.0 $\mathrm{m\,s^{-1}}$, and energy density over 20 $\mathrm{kW\,m^{-2}}$ (Liu et al., 2011). In the U.K., the extractable resource is estimated to be up to 18 TW hyear (Galloway et al., 2014). Some potential sites where maximum current speeds could exceed 2.5 $\mathrm{m\,s^{-1}}$ are also identified in Korea (Kim et al., 2012).

Currently several prototype tidal turbines are tested at specific sites. Some blade failures of the test tidal turbines have been reported (White, 2011; CBCNews, 2010; Shulman, 2008), which are believed to be caused by uncertain loads on the blades. The unsteady hydrodynamic conditions, such as turbulent inflow or free surface waves, would induce complex unsteady loads on the submerged turbines. The majority of previous studies have concentrated on the loads and power production of tidal turbines under steady conditions (Batten et al., 2006; Bahaj et al., 2007; Batten et al., 2008). The knowledge of the unsteady hydrodynamic loads are still very limited. As a result, large safety factors in extreme loads prediction are used to account for the uncertainties in the loads, which would potentially increase the cost of tidal turbines.

Surface waves which can penetrate the water column to a depth of half of the wave length is one important part of unsteady hydrodynamic loads. In order to produce more power, tidal turbines are designed with increasing size, and are expected to be moved into more energetic waters where it would being exposed to significant waves. The cyclic surface wave loads which would undoubtedly not only lead to increase of the extreme loads but also accelerate fatigue of the rotor and blades need to be paid more attention in the design. The assessment of unsteady loads become essential for avoiding unexpected failures of tidal turbines.

Investigations into the effects of turbulent inflow conditions on tidal turbines were carried out by Maganga et al. (2009) and Mycek et al. (2014) considering the turbulence intensities from 3% to 25% of the inflow. Milne et al. (2015) presented experiments to measure unsteady bending moment at the blade root for a scaled tidal turbine subjected to an unsteady planar forcing in a towing tank. Current number $\mu = \tilde{u}/U$ and reduced frequency $k = \pi f c/V$ at the span-wise location of $0.75R$ are used to describe the degree of unsteadiness of the inflow, where $\tilde{u}$ is the amplitude of the velocity perturbation, U is the mean inflow velocity, f is the physical frequency of the flow, c is the local blade chord, and V is the resultant local inflow velocity. They found that the unsteady blade loads increased with frequency and exceed the steady loads by up to 15% when $\mu = 0.10$ and $k \leq 0.05$.

Only a few efforts have been made to study the surface wave effects on tidal turbines. Barltrop et al. (2007) carried out the experiments using a 400 mm diameter rotor in a towing tank with the presence of regular waves. The average thrust and torque was independent with wave frequencies or wave heights. However significant cyclic variation of the loads were observed. The relatively small rotor in Barltrop's study limited the Reynolds number to only about 0.8×10^5 (at 75% blade radius) when the device was towed at $1.0\,\mathrm{m\,s^{-1}}$. The model turbines with small Reynolds number would reduce the unsteady hydrodynamic loads compared to that expected at full-scale with Reynolds number of 1.0×10^6 (Shyy et al., 2007). Similar model tests in a towing tank were reported by Lust et al. (2013) and Luznik et al. (2013). They both confirmed that the average power and thrust were not affected by the passing waves. In Luznik's experiments, the model turbine was towed at $0.6\,\mathrm{m\,s^{-1}}$, whilst being exposed to the regular waves with period of 1.78 s, and height of 7.6 cm. The corresponding reduced frequency k and current number μ is about 0.04 and 0.1, respectively. Their results showed a strong correlation between measured torque and vertical wave particle velocity. Galloway et al. (2014) investigated the wave effects on a 800 mm 3-bladed horizontal axis TST device in regular waves, which was being towed at $0.9\,\mathrm{m\,s^{-1}}$. They also found that the presence of waves did not affect the time averaged torque and thrust, but it caused the cyclic loading with a variation of 37% and 35% of the mean for thrust and torque, with corresponding reduced frequency $k = 0.03$ and current number $\mu = 0.08$.

The mentioned studies have concluded some characteristics of the wave loads on tidal turbines. However only one or some separate regular waves were involved. More experimental data with a wide range of incident waves are needed both for a more general understanding of the surface wave effect on tidal turbines, and for calibration of the parameters in the numerical models.

Several tools have been developed to predict the loads and power output of tidal turbines with different numerical approaches. The tidal turbine problems share some feature of wind turbine calculation. The classical Blade Element Momentum (BEM) theory (Glauert, 1935) is widely used for estimation of the loads on tidal turbines. The steady thrust and torque can be predicted well by the BEM theory compared to experiments (Batten et al., 2008). In order to simulate the time behavior of the loads on tidal turbines, the BEM theory was enhanced with dynamic inflow model and dynamic stall model, such as CACTUS with the free vortex model (Murray and Barone, 2011), AeroDyn with the generalized dynamic wake (GDW) model (Moriarty and Hansen, 2005), and the code with prescribed wake model (Coton and Wang, 1999). To provide more accurate relations between induced velocity and radial circulation distribution especially for the heavy load blades, Epps and Kimball (2013) proposed the unified lifting line theory for performance calculation of tidal turbines. Jo et al. (2012); Zhang et al. (2015) and more recently Tatum et al. (2016) used the Computational Fluid Dynamics (CFD) method to predict both steady- and unsteady-state behavior of tidal turbines bring more realistic and detailed flow features around the submerged rotor.

Most of the numerical approaches mentioned above cannot account for dynamic inflow conditions or incident waves. Faudot and Dahlhaug (2012) used a quasi-static BEM model to predict wave loads on the blades, in which the surface wave effect, as a first order approximation, simply act as an addition to a uniform stream velocity from linear wave theory. Galloway et al. (2014) developed a modified BEM code using Boeing-Vertol dynamic stall model and Pitt-Peters dynamic inflow model, which had good agreement with the towing experiment results. It has to be pointed out that due to the presence of free surface, under some wave conditions, the blade tip would have an opportunity to partly go out of water. It would induce impact loads on the blade and also affect the power production of the tidal turbine. The partly going-out-of and re-entry water process can not be considered and described by available numerical models. It should be paid attention as another aspect of surface wave effects.

In light of above, we developed a new numerical model and carried out a set of experiments to contribute to a more fundamental understanding of the surface wave effect on tidal turbines. The numerical model has been developed and verified for wave load prediction based on the modified BEM theory with an inclusion of added mass effects, wave excitation forces and a one degree-of-freedom (DOF) simulation for turbine rotational motion. Experiments for validation on a 1:25 scaled tidal turbine were also performed in a towing tank, involving regular waves with periods from 1.0 s to 3.0 s and heights from 5.0 cm to 15.0 cm.

2. Development of the numerical model

The Blade Element Momentum (BEM) theory is widely used for the prediction of steady hydrodynamic performance of tidal turbines. The fundamental scheme and modification of the classical BEM model particular for tidal turbines can be found in Molland et al. (2004) and Batten et al. (2008). Some efforts were made by Faudot and Dahlhaug (2012) and Galloway et al. (2014) to include wave-induced load prediction in an unsteady BEM model as mentioned above. In the present paper, the numerical model was also in the framework of the BEM theory with consideration of body motion simulation, added mass effects and wave excitation forces.

2.1. Coordinate systems

When accounting for the surface wave effects, the absolute position in global coordinate of each blade element needs to be known. The undisturbed current velocity and additional wave particle velocity need to be transformed to each blade element as an input to the BEM model at every time step.

The two rectangular coordinate systems as shown in Fig. 1 are used in this paper. An inertial global coordinate system ($OX_0Y_0Z_0$) is centered at the sea bed. Z_0 is the horizontal coordinate, and X_0 is the vertical one. The local coordinate system for each blade ($OXYZ$) is centered at the hub. X is aligned with the rotating blade, and the axis

OZ is located in the plane OX_0Z_0. Then the position vector $\mathbf{X_0}$ in the global coordinate can be transferred into the local blade coordinate as $\mathbf{X}$ by:

$$\mathbf{X} = \mathbf{a_{01}} \cdot \mathbf{X_0} \tag{1}$$

$$\mathbf{a_{01}} = \begin{bmatrix} \cos\theta_{wing} & \sin\theta_{wing} & 0 \\ -\sin\theta_{wing} & \cos\theta_{wing} & 0 \\ 0 & 0 & 1 \end{bmatrix} \tag{2}$$

where $\mathbf{a_{01}}$ is the transformation matrix between the two coordinate systems, and θ_{wing} is the azimuthal position of the blade as defined in Fig. 2.

The position vector $\mathbf{r_i^n}$ of the i-th element on the n-th blade in the global coordinate is determined by equation 3, and the resultant velocity seen by each blade element is found by transforming the velocity $\mathbf{V}$ to the local coordinate by equation 1.

$$\mathbf{r_i^n} = \begin{bmatrix} x_{pi}^n \\ y_{pi}^n \\ z_{pi}^n \end{bmatrix} = \mathbf{r_t} + \mathbf{r_s} + \mathbf{r_{bi}^n} \tag{3}$$

where, $\mathbf{r_t} + \mathbf{r_s}$ is the position vector of the rotor center, and $\mathbf{r_{bi}^n} = \mathbf{a_{01}}^{-1} \cdot [x, 0, 0]^T$ is the vector between the blade element and the rotor center in the global coordinate.

2.2. *Description of free surface waves*

Based on the linear wave theory, incident wave velocity potential ϕ_0, free surface elevation η, and wave particle velocity V_x^{wave} and V_z^{wave} are given in global coordinate system as follows (Faltinsen, 1993):

$$\eta = \zeta_a \sin(\omega_e t - kz) \tag{4}$$

$$\phi_0 = \frac{g\zeta_a}{\omega} \frac{\cosh kx}{\cosh kh} \cos(\omega_e t - kz) \tag{5}$$

$$V_x^{wave} = \omega\zeta_a \frac{\sinh kx}{\sinh kh} \cos(\omega_e t - kz) \tag{6}$$

$$V_z^{wave} = \omega\zeta_a \frac{\cosh kx}{\sinh kh} \sin(\omega_e t - kz) \tag{7}$$

where ζ_a is the wave amplitude, ω is the natural wave frequency, k is the wave number, h is the water depth, and ω_e is the encounter frequency due to the Doppler shift which is defined in equation 8.

In reality, the waves travel on the moving reference frame at the velocity of mean current. Due to the fact that the tidal turbine is fixed, the Doppler shift is caused by the moving reference frame. However in the towing experiments, the waves travel on still water, but the tidal turbine was towed at the velocity of mean current. The Doppler shift in this situation is caused by the moving observer.

$$\omega_e = \omega + kV \tag{8}$$

where V is the undisturbed mean current velocity in reality, or is the towing speed in experiments.

The wave particle velocity is regarded as a perturbation of the mean current velocity in the present numerical model. The total inflow velocity will be transferred into the local element coordinate as follows:

$$\mathbf{V_I} = \mathbf{a_{01}}(\mathbf{V} + \mathbf{V^{wave}}) \tag{9}$$

2.3. Velocity triangle and dynamic wake model

The relative velocity $\mathbf{V_{rel}}$ in the local reference system is defined in equation 10 and shown in Fig. 3. Then the angle of attack α can be computed by equation 12 if the induced velocity $\mathbf{W}$ is known.

$$\mathbf{V_{rel}} = \mathbf{V_I} + \mathbf{V_{rot}} + \mathbf{W} \tag{10}$$

$$\begin{bmatrix} V_{rel,y} \\ V_{rel,z} \end{bmatrix} = \begin{bmatrix} V_y \\ V_z \end{bmatrix} + \begin{bmatrix} -\Omega x \\ 0 \end{bmatrix} + \begin{bmatrix} W_y \\ W_z \end{bmatrix} \tag{11}$$

$$\alpha = \arctan \frac{-V_{rel,y}}{V_{rel,z}} - \beta \tag{12}$$

where β is the blade pitch angle as shown in Fig. 3, $\mathbf{V_0}$ is the inflow velocity due to current and waves seen by the blade section, $\mathbf{V_{rot}}$ is the blade rotating speed, and $\mathbf{W}$ is the induced velocity.

The essence of the BEM numerical procedure is to obtain the induced velocity $\mathbf{W}$. In view of the classical BEM model, the induced velocity is determined by the change of fluid momentum passing the rotor which is considered as an ideal disc. Prandtl's Tip and Hub loss correction is used accounting for the rotor with finite number of blades, and Glauert correction is for high induction factor (Glauert, 1935).

In view of the changes of the inflow caused by the incident waves, the induced velocities on the blade section cannot instantly establish the new steady state conditions. To describe the development of the induced wake field in time domain, the dynamic wake model is introduced. The incident wave periods in the present experiments is from 1.0 s to 1.6 s in model scale. For this condition, the dynamic effects of the wake were limited. A simple model proposed by Øye (1991) is utilized in this paper, in which two first-order differential equations govern the induced velocities (see Equations 13 and 14). It is noted that the Equations 13 and 14 must be solved iteratively since the angle of attack depending on the induced velocity itself. For the unsteady BEM model here, time is used as relaxation. After the blades moved an azimuthal angle in one time step, values from the previous time step are used on the right-hand side of Equations 13 and 14 for updating the new induced velocity (Hansen, 2013). The present dynamic wake model was originally developed for wind turbines. It cannot account for the situation that the blade partly going-out-of and re-entry of water for tidal turbines, and the existence of free surface. From the results and discussions, we know that it caused under-prediction of the dynamic loads. More accurate wake model accounting for the presence of free surface is the authors' future work.

$$W_{int} + \tau_1 \frac{\mathrm{d}W_{int}}{\mathrm{d}t} = W_{qs} + k\tau_1 \frac{\mathrm{d}W_{qs}}{\mathrm{d}t} \tag{13}$$

$$W + \tau_2 \frac{\mathrm{d}W}{\mathrm{d}t} = W_{int} \tag{14}$$

where W_{qs} is the quasi-static value, W_{int} is an intermediate value, τ_1 and τ_2 are two time constants given by (Hansen, 2013):

$$\tau_1 = \frac{1.1}{1 - 1.3a} \cdot \frac{R}{V_0} \tag{15}$$

$$\tau_2 = \left(0.39 - 0.26\left(\frac{r}{R}\right)^2\right) \cdot \tau_1 \tag{16}$$

where, a is the axial induction factor, R is the blade radius, and V_0 is the velocity seen by the blade element.

2.4. Dynamic stall model

The angle of attack at each blade element is oscillating with the waves passing and blade rotating. Dynamic stall may occur as results of the fluctuations of velocity over the rotor plane depending on the angle of attack. For dynamic inflow condition induced by surface waves, in the present experiments, the reduced frequency is no more than 0.05, and the TSR of the rotor is about 5 to 6. It is noted that the stall effects may be insufficient (Galloway et al., 2014). Therefore, only the correction for lift coefficient is considered in this paper (Hansen et al., 2004).

$$C_l = f_s C_{l,inv}(\alpha) + (1 - f_s) C_{l,fs}(\alpha) \tag{17}$$

$$\frac{\mathrm{d}f_s}{\mathrm{d}t} = \frac{f_s^{st} - f_s}{\tau} \tag{18}$$

where $C_{l,inv}$ is the attached lift coefficient, $C_{l,fs}$ is fully separated value, and f_s describe the degree of separation. f_s^{st} is the static value of f_s which is determined by the 2D hydrofoil data. The f_s is assumed to always try to get back to the static value. As the same with the dynamic wake model, the correction for lifting coefficient is also not valid when the blade element goes out of water.

2.5. Hydrodynamic forces on the blade section

The hydrodynamic forces on the blade element considered in this paper are shown in Fig. 3. Based on the slender body assumption, the 3D forces on the blade can be calculated from the integral of the 2D forces acting on the span-wise blade elements (Faltinsen, 1993). In view of the fact that effective reduced frequency is under 0.04 (see Table 3) in this paper, the unsteady effects of lift force associated with the varying local angle of attack or inflow velocity are ignored (Leishman, 2002). The hydrodynamic forces acting on the blade are considered separately and combined through superposition of lift and drag forces, excitation forces, and added mass forces.

The lift and drag forces on each blade element are decided by the 2-D lift and drag coefficients and are proportional to the square of the relative velocity:

$$L = \frac{1}{2}\rho V_{rel}^2 c C_l^{(2D)} \tag{19}$$

$$D = \frac{1}{2}\rho V_{rel}^2 c C_d^{(2D)} \tag{20}$$

where ρ is the water density, c is the local chord, V_{rel} is the relative velocity determined by equation 13, and $C_l^{(2D)}$ and $C_d^{(2D)}$ are the local lift and drag coefficients respectively, which were calculated by the panel code XFOIL and compared with the experimental data from Molland et al. (2004).

Generally, the excitation force can be given by:

$$-F_{ext}^{(2\mathrm{D})} = (\rho A + m^{(2D)})\frac{\mathrm{d}V_{rel}}{\mathrm{d}t} \tag{21}$$

where A is the area of the blade section, $m^{(2D)}$ is the 2D added mass for the blade section, and V_{rel} is the relative velocity seen by the blade element. The time derivative term can be decomposed based on equation 10 as follows:

$$\frac{\mathrm{d}V_{rel}}{\mathrm{d}t} = \frac{\mathrm{d}V}{\mathrm{d}t} + \frac{\mathrm{d}W}{\mathrm{d}t} + \frac{\mathrm{d}V^{wave}}{\mathrm{d}t} \tag{22}$$

where V is the mean current velocity regarded as a constant ($\mathrm{d}V/\mathrm{d}t = 0$), W is the induced velocity obtained by the dynamic wake model, and V^{wave} is the wave particle velocity at the rotor plane.

The wave excitation force F_{wave} on a single blade element consisting of Froude-Kriloff force $F_{wave,z}^{\mathrm{FK}}$ and diffraction force $F_{wave,z}^{\mathrm{D}}$ is given both in the z and y directions. The drag term in wave excitation force is ignored.

$$F_{wave,z} = F_{wave,z}^{\mathrm{FK}} + F_{wave,z}^{\mathrm{D}} = -(\rho A + m_z^{(2D)})\frac{\partial}{\partial t}\Big(\frac{\partial \phi_0}{\partial z}\Big) \tag{23}$$

$$F_{wave,y} = -(\rho A + m_y^{(2D)})\frac{\partial}{\partial t}\Big(\frac{\partial \phi_0}{\partial y}\Big) \tag{24}$$

where ϕ_0 is the incident wave velocity potential.

The force F_{induce} associated with acceleration of the wake is determined by the time derivative of the induced velocity given by the dynamic wake model. To avoid numerical instability, and in view of the fact that the $F_{induce,z}$ is much smaller than the lift force, F_{induce} is not coupled to affect the wake in return. In other words, the wake acceleration is only dependent on the lift.

$$F_{induce,i} = (\rho A + m_i^{(2D)})\frac{\mathrm{d}W_i}{\mathrm{d}t} \tag{25}$$

where i donates the y or z direction.

The added mass forces caused by the moving body can be given by:

$$-F_a^{(2\mathrm{D})} = m^{(2D)}\frac{\mathrm{d}^2X}{\mathrm{d}t^2} \tag{26}$$

where X represents the blade element position. The turbine in z direction is motionless, and the blade rotation in y direction is considered. Hence the acceleration term in y and z directions are given separately by:

$$\left.\frac{\mathrm{d}^2X}{\mathrm{d}t^2}\right|_z = 0 \tag{27}$$

$$\left.\frac{\mathrm{d}^2X}{\mathrm{d}t^2}\right|_y = x\frac{\mathrm{d}\Omega}{\mathrm{d}t} \tag{28}$$

The added mass moment can be given in y direction as follows:

$$M_{\Omega,y} = m_y^{(2D)}x\frac{\mathrm{d}\Omega}{\mathrm{d}t} \tag{29}$$

Several previous studies have also modelled and investigated the added mass effects. Maniaci and Li (2012) investigated the added mass effects for the rapid pitching cases, and the results indicated that the added mass had a noticeable influence on blade loads. Whelan (2010) concluded that the unsteady hydrodynamic loading was in-phase with inflow velocity and the added mass effects were small for low reduced frequency cases. It is hard to measure the added mass force in experiments directly. From previous studies and the results presented in the following, we also believed that the added mass effects are limited for the present small incident waves. Although the implementation of added mass has not shown important effects on the load for present conditions, we believed that for elastic blades (combined with a hydroelastic model of the blades) or cases with rapid pitch motions, the added mass implementation would be relevant. Here, as the first step of our work, the added mass model was considered.

The hydrodynamic torque and thrust on the rotor is obtained by the sums of force components on every blade element:

$$T = \sum_n^B \sum_i^N \left(L_i^n \cos\phi_i^n + D_i^n \sin\phi_i^n + F^n_{wave,z,i} - F^n_{z,induce,i}\right)\Delta x_i^n \tag{30}$$

$$M = \sum_n^B \sum_i^N \left((L_i^n \sin\phi_i^n - D_i^n \cos\phi_i^n + F^n_{wave,y,i} - F^n_{induce,y,i})x_i^n - M_{\Omega,y}\right)\Delta x_i^n \tag{31}$$

where i and n donate the i-th blade element on n-th blade, B is the total number of the blades, N is the total number of elements on each blade, x_i^n is the element radial position, and Δx_i^n is the span-wise length of each element.

Among the hydrodynamic forces acting on the blade section, the lift and drag forces are proportional to the square of the relative velocity, and the excitation forces are proportional to acceleration of the relative velocity which is caused by passing waves in this study. The period of acceleration of the relative velocity is equal to the wave period, and the amplitude of that is proportional to the wave height. Based on linear wave assumption, the waves are small perturbations on the free surface. Therefore, the amplitudes of the excitation forces are small compared with the lift force. From the energy point of view, the excitation and added mass forces are conservative. Without consideration of the second-order effects, the power production of the turbine is only related to the lift and drag forces.

Due to the azimuthal symmetry of the blades arrangement, the effects of buoyancy and gravity forces on shaft torque are canceled out. The buoyancy and gravity forces are not included in the present numerical model, but it is significant for evaluating the force on a single blade, which is beyond the scope of the present paper.

2.6. Added mass of the blade section

The above excitation and added mass forces are both related to the added mass of the blade section, which is not considered for the wind turbine due to small air density. However water density is approximate 700 times of air density. The added mass should not be ignored for tidal turbines.

The blade element is assumed to be a 2D flat plate for the estimation of the 2D added mass. Only the $m_{11}^{(2D)}$ in the direction perpendicular to the airfoil chord line as shown in Fig. 4 is considered, and given by:

$$m_{11}^{(2\mathrm{D})} = \frac{1}{4}\rho\pi c^2 \tag{32}$$

$$m_{22}^{(2\mathrm{D})} = 0 \tag{33}$$

where ρ is the water density, and c is the local chord of the blade element.

The $m_{11}^{(2D)}$ is then decomposed into both y and z directions as follows:

$$m_y^{(2D)} = m_{11}^{(2D)} \sin\beta \tag{34}$$

$$m_z^{(2D)} = m_{11}^{(2D)} \cos\beta \tag{35}$$

where β is the blade twist angle.

2.7. Rotor motion simulation and speed control strategy

Most of previous studies assumed that the turbine rotational speed is fixed. In practice, although a controller or regulation system is utilized to restrict the rotational speed, the RPM is still fluctuating due to the cyclic shaft torque. The RPM was directly affected by the passing surface wave, which was observed and recorded in several experiments by Luznik et al. (2013); Galloway et al. (2014). The cyclic RPM would also affected the loads on the blades in turn.

In the present paper, a single degree-of-freedom (DOF) model of the rotor was used to simulate the varying rotational speed of the tidal turbine. The one DOF motion is governed by:

$$I\dot{\Omega} = M - M_G(\Omega) + M_{Control}(t) \tag{36}$$

where Ω is the rotational speed, I is the rotor inertia, M is the hydrodynamic torque given by equation 31, M_G is the generator torque proportional to the square of the rotational speed, and $M_{Control}$ is the feedback control torque determined by a proportional integral derivative controller (PID controller) defined as follows:

$$M_{Control}(t) = K_M\Big(K_p e(t) + K_i \int_0^t e(\tau)\mathrm{d}\tau + K_d \frac{\mathrm{d}e(t)}{\mathrm{d}t}\Big) \tag{37}$$

where $e(t) = \Omega_{\mathrm{SP}} - \Omega(t)$ is the error (Ω_{SP} is the set-point), K_M is the generator stiffness assumed to be a fixed value, K_p, K_i and K_d are the proportional, integral and derivative gains, respectively. The K_p, K_i and K_d are tuned based on the goal of a little overshoot, a proper artificial damping, and small steady-state error by practice.

The integral flow chart of dynamic stall model, dynamic inflow model, added mass effects, linear waves and body motion simulation in time domain is illustrated in Fig. 5. The rotational speed Ω^k and azimuthal position θ_{wing}^k are obtained by solving the motion equation (see equation 36) by Runge Kutta fourth-order method at k-th time step. Then the Ω^k is considered unchanged in one time step and transferred into the unsteady BEM model to calculate the induced velocity W^k and the hydrodynamic loads M^k and T^k on the rotor. Meanwhile, the obtained rotational speed is compared with the set-point in the PID controller to output the control Torque (see equation 37) for next time step. Next all these loads formed the right hand terms in the motion equation to determine a new rotational speed Ω^{k+1} and azimuthal position θ^{k+1}_{wing} for the next time step.

3. Experimental set-up and method

3.1. Towing tank

Experiments were carried out in the towing tank at Zhejiang Ocean University, China. The towing tank as shown in Fig. 6 is 130 m long, 6 m wide and 3 m deep. A flap-type wave generator is at the upstream end of the tank, and a passive wave-absorbing beach is located at the other end with the damping grids for passive wave dissipation. The carriage velocity was controlled by the computer. For each run, the carriage speed up with constant acceleration at the begin, and then maintained the velocity during the test before finally slowing down in the present towing experiments.

3.2. Model tidal turbine

A horizontal-axis, 3-bladed tidal turbine as shown in Fig. 7 was used in this study. Choosing a larger size rotor is helpful for maximizing the Reynolds number. However, due to the constraints such as the blockage of the tunnel, the ability of speed control of the motor, range of dynamometer, and processing difficulty of the aluminum alloy blade, the diameter of the rotor was chosen to be 800 mm as a compromise. There have been few experiments on tidal turbine with larger rotor than the present. In the present paper, Froude scaling was the dominant scaling parameter. The 1 : 25 scaled model represented a 20 m-diameter, 1 MW prototype tidal turbine developed by Shanghai Jiao Tong University for deep-water tidal current energy exploitation. The blockage of the tunnel was less than 3.0%. No blockage correction to the experimental data was applied (Galloway et al., 2014; Milne et al., 2015). Although increasing towing speed is also effective for increasing the Reynolds number, the inflow velocity at full scale should be reasonable for tidal turbine sites under Froude scaling.

The unsteady behavior of the hydrodynamic loads related to Reynolds number may have some differences between model and prototype. In this paper, all the results from experiments are shown and discussed at model scale. Meanwhile, the numerical analysis as comparison was also done at model scale. All the structures were treated to be rigid both in experiments and numerical predictions. The hydro-elastic problem is beyond the scope of this paper.

The hub diameter was 100 mm. The blade sections were developed from NACA 63-8xx profile with varying thickness and pre-twist. The span-wise distribution of the chord, pre-twist and thickness is shown in Table 1 at model scale.

3.3. Test rig

The test rig as illustrated in Fig. 9 mainly consisted of an airfoil section tank, a generator/motor, a dynamometer, and a 3-bladed rotor. The generator/motor was equipped with close-loop controller to ensure precise speed control. The dynamometer was utilized to record the torque and thrust on the end of the shaft. The whole test rig was connected to the main carriage which could move forward and back in the tank with a given velocity, meanwhile the rig could be moved up and down to adjust the submergence of the turbine hub from 0.32 m to 0.96 m to satisfy different test conditions. A wave probe as shown in Fig. 8 was located in front of the main carriage to record incident wave heights. The wave heights at the rotor plane were obtained by changing the phase of the measured waves. All these mentioned instruments were carefully calibrated before the experiments. All the quantities were recorded with a sampling rate of 100 Hz.

3.4. Regular wave generation

A flap-type wave generator was used to generate regular waves at the upstream end of the towing tank in this study. The typical tidal turbine sites are often located at the channels between the islands near coast. The waves tend to have long periods and relatively small significant wave heights in these sheltered location. The real wave data from observation at these sites are limited. Therefore the selected regular waves cover a wide period range from 1.0 s to 3.0 s in model scale, corresponding to prototype periods from 5.0 s to 15.0 s in order to get the load RAOs from regular wave experiments. The wave length was from 1.56 m to 12.68 m. Table 2 shows that the ratio λ/h is from 0.52 to 4.22. These regular waves can be split into deep waves and intermediate waves by a criteria of $\lambda/h = 2$. The wave height was determined by a steepness that did not exceed 3.5%.

The reduced frequency and current number of some typical cases are listed in Table 3. Due to the non-uniformity of the inflow distribution caused by the passing waves and rotating blade at rotor plane, the reduced frequency k at 0.75% radius and current number μ at the hub height were used to describe the degree of unsteadiness of the inflow. In the present study, the reduced frequency k is between 0.02 and 0.04, and the current number is under 0.2. Relatively small reduced frequency ($\approx O(0.01)$) ensured that changes in the angle of attack was small. The maximum wave induced horizontal velocity at hub height was under 20% of the mean current velocity, which kept the assumption reasonable that the wave particle velocities are treated as perturbations on the main current velocity.

All the selected waves have been calibrated before the experiments. The parameters of the calibrated waves are shown in Table 2. A fixed wave probe was placed at the center of the towing tank about 50 m away from the upstream wave maker for the wave calibration. The selected time histories of the incident wave elevation with different wave periods are shown in Fig. 10. Although all the waves have been calibrated, the encounter waves in each run had a little differences compared with the calibrated waves. All the analysis were based on the measured loads and corresponding encounter waves recorded in each run.

4. Results and discussion

4.1. Average power and thrust coefficients

The time averaged C_p and C_T for both still water cases and wave cases were presented as the first step of validation. The experimental C_p and C_T points versus tip speed ratio (TSR) are shown and compared with the numerical prediction in Figs. 11 and 12 . The C_p, C_T, and TSR are defined as follows:

$$C_p = \frac{M\Omega}{0.5\rho U^3 \pi R^2} \tag{38}$$

$$C_T = \frac{T}{0.5\rho U^2 \pi R^2} \tag{39}$$

$$\mathrm{TSR} = \frac{\Omega R}{U} \tag{40}$$

where M is shaft torque, T is thrust, Ω is rotational speed, U is carriage velocity, ρ is water density, and R is the rotor radius.

The still water cases (no wave cases) were performed at the carriage velocity of $0.56\,\mathrm{m\,s^{-1}}$ and $0.68\,\mathrm{m\,s^{-1}}$, and the rotor speed from 65 RPM to 138 RPM. The submergence of the turbine hub is 0.64 m (0.8D). The C_p and C_T curves have been well discussed by previous studies (Bahaj et al., 2007; Milne et al., 2015). At the low speed region (TSR$<$ 4), due to the fixed pitch angle, the rotor is dominated by the stall effects. When the TSR is larger than 7, the turbulent wake state leads to a reduction of the power coefficient. The optimal power coefficient is obtained at TSR approximately 5 to 6. As a result, most of the wave cases in this paper were performed in this optimal TSR region.

In view of Froude scaling, the carriage velocities of $0.56\,\mathrm{m\,s^{-1}}$ and $0.68\,\mathrm{m\,s^{-1}}$ are equivalent to $2.8\,\mathrm{m\,s^{-1}}$ and $3.4\,\mathrm{m\,s^{-1}}$ in prototype respectively, which are the typical rated current speed for tidal turbines. The Reynolds number, based on the cord length and the maximum relative velocity at 75% radius in model scale was between 0.87-1.52×10^5 in the present cases, which was lower than that of the prototype tidal turbines ($\sim O(10^6)$). The model turbine with lower Reynolds number would reduce the dynamic effects acting on the blade compared with that expected in full-scale (Shyy et al., 2007). The previous studies also confronted the situation with this dilemma of Reynolds number (Barltrop et al., 2006; Luznik et al., 2013; Galloway et al., 2014; Milne et al., 2015). Therefore, all the experimental data and numerical predictions were discussed in model scale in this paper.

The wave cases were performed under the same towing conditions but being exposed to different incident waves. Several previous experiments indicate that the passing waves did not affect the time averaged loads and power output (Faudot and Dahlhaug, 2012; Luznik et al., 2013; Galloway et al., 2014). The results from the wave cases have some differences in the present C_p and C_T curves. This may be caused by the following reasons.

The first one could be the mean drift effects of the waves which may cause shift of the mean value for some cases. The thrust force and the torque on the tidal turbine are the resulting force and moment from the lift and the drag forces acting on each blade cross-section, which are quadratic terms of the local velocity. Considering both the current velocity (which is dominating) and the wave particle velocity at each blade cross-section, we will get the thrust and the torque with linear and second-order terms with respect to the wave induced velocity. The lift and drag forces acting on a blade section in waves can be simply written as $F \propto (U_0 + V_w)^2$. It can be further split into three parts: $F_0 \propto U_0^2$ which is the mean force; $F_w^1 \propto 2U_0V_w$ which is the linear wave induced loads; and $F_w^2 \propto V_w^2$ which is the second-order effects (mean drift effects). In present, the authors cannot given second-order transfer functions to quantitative explanation of this effects, which will be the future work of the authors.

Another reason may be related to the generator speed. In experiments, although the generator speed is close-loop controlled, for very slow or fast speed, the speed control is not perfectly effective. The varying rotational speed may cause errors for waves cases.

4.2. Comparisons of the experimental data and numerical simulation

The typical wave test procedure is presented as follows. Firstly, the motor driven the turbine to rotate at the given speed without forward velocity and waited for the incident waves coming from the upstream end of the tank. As the waves arrive, the carriage started to speed up and then maintained the constant velocity. Finally, it stopped before the tank end after more than 25 wave periods.

The experimental time histories of the shaft torque and thrust from a case ($U = 0.68\,\mathrm{m\,s^{-1}}$, RPM = 94.2, $T_{wave} = 1.6\,\mathrm{s}$, $H_{wave} = 7\,\mathrm{cm}$, and submergence of the hub is 0.64 m) is presented as an example in Fig. 13. The numerical results have very good agreement with experimental data. It is shown that the passing waves directly affect the RPM, torque and thrust of the rotor by inducing cyclic oscillations. The relation between the encounter wave elevation at the rotor plane and the RPM, torque and thrust shows that the waves and its effects on these quantities have the same frequency and very small phase differences. When the wave elevation at the rotor plane reached the highest level, the wave particle had maximum forward speed, and hence it caused the maximum loads on the rotor, and vice versa. However, only wave frequency oscillation could be observed from the time histories of the shaft torque and thrust. This was due to the three blades are at symmetrical azimuthal positions, and it would cancel the 1P effects. The wave induced oscillation of the shaft torque in-turn influenced the quality of the electrical power production.

From above discussion, we know that the waves mainly cause the periodical oscillations with wave frequency on the loads. The average range of the dynamic torque M^{WAVE} and thrust T^{WAVE} (see equations 41 and 42) are used to describe the degree of the effects caused by the passing waves in this paper.

$$M^{\text{WAVE}} = \sum_{1}^{N} M_i^{\text{range}} \Big/ N \tag{41}$$

$$T^{\text{WAVE}} = \sum_{1}^{N} T_i^{\text{range}} \Big/ N \tag{42}$$

where M_i^{range} and T_i^{range} are the range of the dynamic torque and thrust in a single period, and N is the selected number of the periods, which is normally no less than 10.

4.3. Wave effects on torque and thrust

It is shown that M^{WAVE} and T^{WAVE} have linear dependence on the incident wave height (see Fig. 14 (a), (b) and (c)). In this set of the cases, the same towing condition was held at $U = 0.68\,\text{m}\,\text{s}^{-1}$, RPM = 87.6 (TSR = 5.4), and submergence of the hub is 0.64 m (0.8D). The numerical results are lines in the figures as expected with the linear incident waves. Experimental results agree well with the numerical prediction. Figure 14 (d), (e) and (f) show the M^{WAVE} and T^{WAVE} normalized by its mean value versus instantaneous current number. It is noted that a small perturbation of the inflow (about 15% of the mean) could induce large amplitude of the cyclic variation of the loads (about 50% of the mean loads).

Due to the linear relationship between the incident waves and load responses, the load RAOs can be introduced to investigate the feature of responses in frequency domain. The torque and thrust RAOs are defined and nondimensionalized as follows:

$$k_M = \frac{M^{\text{WAVE}}}{0.25\rho g D^3 \zeta_a} \tag{43}$$

$$k_T = \frac{T^{\text{WAVE}}}{0.25\rho g D^2 \zeta_a} \tag{44}$$

where ρ is water density, g is the acceleration of gravity, D is the diameter of the rotor, and ζ_a is the amplitude of the incident waves. It should be pointed out that the RAOs are only valid for linear incident waves or for the conditions that current number $\mu \leq 0.2$ and reduced frequency $k \leq 0.04$.

Figures. 16 and 15 show the numerical and experimental results of the nondimensional responses in frequency domain with different submergence H/D. The response curve of torque agrees very well with the numerical predictions. But there are discrepancies in the thrust curve for $H/D = 0.6$. This discrepancy was due to the possible dynamic effects of the model turbine in the experimental set-up in some cases.

In Figs. 16 and 15, the time averaged power or thrust coefficients are also shown. For the same towing velocity and rotation speed, the mean value for cases with different wave conditions is unchanged. Similar results for the mean power and thrust coefficients were also presented in previous studies (Faudot and Dahlhaug, 2012; Luznik et al., 2013; Galloway et al., 2014).

For $\lambda/h < 0.2$ (h is the water depth), V_z^{Wave} decreases exponentially with increasing depth (see Fig. 17 (a)). The short wave effects are strictly restricted in very limited depth, and we can just put the tidal turbine under the wave influence region ($H > \lambda/2 + 0.5D$) to avoid effect of waves. If submergence of the hub $H/D = 0.8$, it means that the waves with $\lambda/h < 0.16$ cannot have significant influence on the tidal turbine. Therefore increasing submergence is an effective way to avoid effects from deep-water waves. On the other end, when wave length goes to zero, the dynamic response of the torque and thrust also vanish converting to corresponding still water cases.

For $0.2 < \lambda/h < 4$, with the increasing wave length, submergence and incident wave frequency become important factors in the response curves. The wave influence region is so large that there are no more space to avoid the effects completely (see Fig. 17 (b)). When $\lambda/h < 1$, the load responses (torque and thrust) go up sharply with increasing wave length. When the submergence H/D is less than 0.8, a response peak can be identified around $\lambda/h = 1$ in both torque and thrust curves. After that, the responses tend to a fixed value slowly and smoothly. For the intermediate waves, the submergence of the turbine becomes important. The appearance of the response peak is also related to submergence, and will be discussed later.

For $\lambda/h > 4$, the water particle has almost the same horizontal velocity V_z^{Wave} throughout the whole water column (see Fig. 17 (c)). The submergence is not the key factor any more. The torque and thrust slowly tend towards a fixed value with continually increasing wave length. It is interesting to note that the response of very long waves provides a convenient and effective method to evaluate the wave effects on the tidal turbine. The period of the incident waves also become very long. When the reduced frequency $k < O(0.01)$, the flow can be assumed steady or quasi-steady (Leishman, 2002). Although we can estimate the response by performing incident waves with period long enough or just by interpolation of the response curves, the quasi-static method will be introduced later as an alternative way to calculate the quasi-static response of dynamic thrust and torque.

4.4. Free surface and TSR effects

As shown previously, we know that the response peak occurs around $\lambda/h = 1$, and submergence is the key factor of the load response caused by intermediate waves. Therefore, two incident waves with $\lambda/h = 0.75$ and 1.33 were selected to investigate the submergence effects. The non-dimensional response of dynamic torque as a function of submergence of the hub is shown in Fig. 18. When $H/D < 0.7$, the numerical and experimental results agreed very well. From Fig. 17, it shows that the maximum current number μ is less than 0.2 in this situation. The numerical model with linear wave assumption worked pretty well. With the increasing submergence of the hub, the dynamic response also decreased, which means that larger submergence would be helpful for limiting wave induced loads on the rotor. The lower limit as shown in Figs. 16 and 15 could be obtained by the physical limitation of the presence of sea bed, that putting the rotor hub only 0.5D up on the sea bed. Under this condition, the effects caused by intermediate waves and deep-water waves can be effectively reduced. The waves are no longer the issue, but the turbine would suffer from the boundary layer of the inflow caused by the sea bed, which is beyond the scope of this paper.

When the rotor getting close to free surface ($H/D < 0.6$), the present numerical model obviously underestimated the wave induced loads from the comparison in Fig. 18. The horizontal wave particle velocity V_z^{Wave} could be larger than 50% of the inflow current velocity, which means that regarding the water particle velocity as a disturbance is no longer suitable. The dynamic wake behind the rotor was strongly affected by the free surface, which was not considered in the present dynamic wake model. Under extreme condition, the tidal turbine blades would have an opportunity to go out of water, bringing more complex physical phenomenon that can not be described by the present numerical model. Therefore, we did not give the upper limit in Figs. 16 and 15. In order to take the free surface effects into account, more details about the free surface should be considered in the numerical model, and it will be the future work for the authors.

The rotational speed of the turbine is another parameter of this problem. Normally, it is determined by the operating point on the power coefficient curve. In this paper, optimal TSR is about 5 to 6 (see Fig. 11). When inflow velocity $U = 0.68\,\mathrm{m\,s^{-1}}$, the optimal rotor speed is from 1.35 Hz to 1.62 Hz, which is obviously higher than the effective incident wave frequency around 0.65 Hz ($\lambda/h = 1$). Therefore the coupling effects between the rotation of the rotor and incident waves can be ignored. The non-dimentional thrust and torque RAOs as a function of λ/h with different TSRs from numerical prediction are shown in Figs. 19 and 20. It is shown that the varying TSR dose not affect much for intermediate waves. However it dose affect the quasi-static value for long waves significantly. The quasi-static torque goes down, but the thrust goes up with increasing rotating speed in this situation. For deciding the operating TSR, the effects of TSR on the wave loads should be taken into account.

4.5. Estimation for the quasi-static k_M^{ST} and k_T^{ST}

From Figs. 16, 15, 19 and 20, we know that when $\lambda \gg h$, the load responses tend towards the quasi-static values which can be called k_M^{ST} and k_T^{ST}. The quasi-static values were proved to be independent with wave conditions or submergence of the rotor, which would be convenient for the prediction of wave loads in early design stage. Here, we provide a method to calculate the quasi-static responses by shallow water assumption.

The relation between the tidal current velocity and shaft torque and thrust at RPM = 87.6 is shown in Fig. 21. The shaft torque M and thrust T can be written as a function of the tidal current velocity V and rotational speed Ω:

$$M = f(V, \Omega) \tag{45}$$

$$T = g(V, \Omega) \tag{46}$$

If the rotational speed Ω is regarded as a constant, a small change of the torque can be given by:

$$\Delta M = f'(V, \Omega)\Delta V \tag{47}$$

where, ΔV is a small change of the inflow velocity induced by the waves. As the wave length is assumed to be infinite, the shallow water condition ($\lambda \geq 20h$) is automatically satisfied. Since the reduced frequency k is smaller than 0.01, the inflow can be regarded as quasi-steady state (Leishman, 2002). The range of the horizontal wave particle velocity is obtained by shallow water condition which is independent with the wave frequency and submergence as follows (Mei et al., 2005):

$$\Delta V = 2\zeta_a \sqrt{\frac{g}{h}} \tag{48}$$

where ζ_a is the wave amplitude, g is the acceleration of gravity, and h is the water depth.

Therefore, the k_M^{ST} and similarly k_T^{ST} can be given by:

$$k_M^{\mathrm{ST}} = \frac{8f'(V, \Omega)}{\rho D^3 \sqrt{gh}} \tag{49}$$

$$k_T^{\mathrm{ST}} = \frac{8g'(V, \Omega)}{\rho D^2 \sqrt{gh}} \tag{50}$$

The k_M^{ST} and k_T^{ST} are related to water depth of the site. It indicates that the deeper site would be helpful for reducing the wave load effects, and tidal turbines should not be located at the extreme shallow waters. The k_M^{ST} and k_T^{ST} can be obtained by the long wave approximation from Figs. 19 and 20, or by the quasi-static method from equations 49 and 50. The results by the two established approaches with different TSRs at mean inflow velocity $U = 0.68\,\mathrm{m\,s^{-1}}$ are listed in Table 4, which shows very good agreements.

5. Conclusions

By performing both numerical and experimental approaches, the objective of this paper is to obtain a fundamental understanding of the surface wave effects on the loads on tidal turbines. A new numerical model based on the modified BEM theory with the inclusion of added mass effects wave excitation forces and a one degree-of-freedom (DOF) simulation for the turbine rotational motion have been developed to simulate the first-order loads on the turbine. Based on the presented experimental results, the contributions to the wave induced loads by added mass, dynamic stall and dynamic wake model are limited. However, this may not be the case for non-stiff blades or extreme loads, which will be the authors' future studies. The experiments on a 1:25 scaled tidal turbine have been carried out in the towing tank at Zhejiang Ocean University, China. The towing speed was $0.56\,\mathrm{m\,s^{-1}}$ and $0.68\,\mathrm{m\,s^{-1}}$. The regular waves with periods from 1.0 s to 3.0 s and heights under 15.0 cm at model scale were generated.

Some conclusions are summarized as follows:

- The numerical prediction agrees well with the experimental data validating the reliability of the present numerical model.
- The regular waves did not affect the average loads and power output from experimental and numerical results. The amplitudes of periodical oscillations of thrust and torque could reach up to 50% of the mean value induced by the passing waves with period of 1.6 s and height of 14 cm. A small perturbation of the inflow (15% of the mean velocity) could induce large amplitude of the cyclic variation of the thrust and torque on the rotor (50% of the mean load).

- For linear incident waves, the amplitude of the cyclic loads have linear dependence on the wave height. The non-dimensional load RAOs k_M and k_T were introduced for estimating the wave loads, which were proved to be sensitive to the submergence and the incident wave frequency. To avoid severe wave load effects, the submergence should be at least 0.8 of the rotor diameter.

- The quasi-static k_M^{ST} and k_T^{ST} independent with the submergence and wave conditions provide an approximate method for evaluating the surface wave effects on tidal turbines, which could be obtained by the long waves approximation (see Figs. 19 and 20) or by the quasi-static method (see Eqns. 49 and 50). The surface wave loads should be carefully considered in the design of tidal turbines.

Acknowledgments

The authors thank Dr. Handi Wei, Xiaona Ge, and Peng Zhu for their contributions in building and executing the model. The present study is supported by National Natural Science Foundation of China (Grant No. 51679137) and the Open Project of the State Key Laboratory of Ocean Engineering, China (Grant No. GKZD010068). Zhejiang Ocean University also provided much support for the experiments. All of the help is greatly appreciated and acknowledged by the authors. The first author also acknowledge the support provided by China Scholarship Council (CSC) for his visiting of Norwegian University of Science and Technology.

References

Adcock, T.A.A., Draper, S., Nishino, T., 2015. Tidal power generation - a review of hydrodynamic modelling. Proceedings of the Institution of Mechanical Engineers Part A-Journal of Power and Energy 229, 755–771.

Bahaj, A.S., Molland, A.F., Chaplin, J.R., Batten, W.M.J., 2007. Power and thrust measurements of marine current turbines under various hydrodynamic flow conditions in a cavitation tunnel and a towing tank. Renewable Energy 32, 407–426.

Barltrop, N., Varyani, K., Grant, A., Clelland, D., Pham, X., 2006. Wave-current interactions in marine current turbines. Proceedings of the Institution of Mechanical Engineers, Part M: Journal of Engineering for the Maritime Environment 220, 195–203.

Barltrop, N., Varyani, K., Grant, A., Clelland, D., Pham, X., 2007. Investigation into wave—current interactions in marine current turbines. Proceedings of the Institution of Mechanical Engineers, Part A: Journal of Power and Energy 221, 233–242.

Batten, W.M.J., Bahaj, A.S., Molland, A.F., Chaplin, J.R., 2006. Hydrodynamics of marine current turbines. Renewable Energy 31, 249–256.

Batten, W.M.J., Bahaj, A.S., Molland, A.F., Chaplin, J.R., 2008. The prediction of the hydrodynamic performance of marine current turbines. Renewable Energy 33, 1085–1096.

CBCNews, 2010. Turbine damage stalls fundy tidal power test URL: [online](June11,2010)http://www.cbc.ca/news/canada/nova-scotia/story/2010/06/11/ns-fundy-tidal-blades.html[accessed25.10.2016].

Coton, F., Wang, T., 1999. The prediction of horizontal axis wind turbine performance in yawed flow using an unsteady prescribed wake model. Proceedings of the Institution of Mechanical Engineers, Part A: Journal of Power and Energy 213, 33–43.

Elghali, S.B., Benbouzid, M., Charpentier, J.F., 2007. Marine tidal current electric power generation technology: State of the art and current status, in: 2007 IEEE International Electric Machines & Drives Conference, IEEE. pp. 1407–1412.

Epps, B.P., Kimball, R.W., 2013. Unified rotor lifting line theory. Journal of Ship Research 57, 181–201.

Faltinsen, O., 1993. Sea loads on ships and offshore structures. Cambridge university press.

Faudot, C., Dahlhaug, O.G., 2012. Prediction of wave loads on tidal turbine blades. Energy Procedia 20, 116–133.

Galloway, P.W., Myers, L.E., Bahaj, A.S., 2014. Quantifying wave and yaw effects on a scale tidal stream turbine. Renewable Energy 63, 297–307.

Glauert, H., 1935. Airplane propellers, in: Aerodynamic theory. Springer Berlin Heidelberg, pp. 169–360.

Hansen, M., Gaunaa, M., Madsen, H., 2004. A beddoes-leishman type dynamic stall model in state-space and indicial formulations, report no. R-1354 (EN), Risø National Laboratory .

Hansen, M.O., 2013. Aerodynamics of wind turbines. Routledge.

Jo, C.H., Yim, J.Y., Lee, K.H., Rho, Y.H., 2012. Performance of horizontal axis tidal current turbine by blade configuration. Renewable Energy 42, 195–206.

Khan, M.J., Bhuyan, G., Iqbal, M.T., Quaicoe, J.E., 2009. Hydrokinetic energy conversion systems and assessment of horizontal and vertical axis turbines for river and tidal applications: A technology status review. Applied Energy 86, 1823–1835.

Kim, G., Lee, M.E., Lee, K.S., Park, J.S., Jeong, W.M., Kang, S.K., Soh, J.G., Kim, H., 2012. An overview of ocean renewable energy resources in korea. Renewable and Sustainable Energy Reviews 16, 2278–2288. URL: http://www.sciencedirect.com/science/article/pii/S136403211200041X, doi:10.1016/j.rser.2012.01.040.

Leishman, J.G., 2002. Challenges in modeling the unsteady aerodynamics of wind turbines, in: ASME 2002 Wind Energy Symposium, American Society of Mechanical Engineers. pp. 141–167.

Liu, H.w., Ma, S., Li, W., Gu, H.g., Lin, Y.g., Sun, X.j., 2011. A review on the development of tidal current energy in china. Renewable and Sustainable Energy Reviews 15, 1141–1146.

Lust, E.E., Luznik, L., Flack, K.A., Walker, J.M., Benthem, M.C.V., 2013. The influence of surface gravity waves on marine current turbine performance. International Journal of Marine Energy 34, 27–40.

Luznik, L., Flack, K.A., Lust, E.E., Taylor, K., 2013. The effect of surface waves on the performance characteristics of a model tidal turbine. Renewable Energy 58, 108–114.

Maganga, F., Germain, G., King, J., Pinon, G., Rivoalen, E., 2009. Experimental study to determine flow characteristic effects on marine current turbine behaviour, in: EWTEC 2009, Uppsala.

Maniaci, D.C., Li, Y., 2012. Investigating the influence of the added mass effect to marine hydrokinetic horizontal-axis turbines using a general dynamic wake wind turbine code. Marine Technology Society Journal 46, 71–78. doi:10.4031/mtsj.46.4.4.

Mei, C.C., Stiassnie, M., Yue, D.K.P., 2005. Theory and applications of ocean surface waves: nonlinear aspects. volume 23. World scientific.

Milne, I., Day, A., Sharma, R., Flay, R., 2015. Blade loading on tidal turbines for uniform unsteady flow. Renewable Energy 77, 338–350.

Molland, A.F., Bahaj, A.S., Chaplin, J.R., Batten, W.M.J., 2004. Measurements and predictions of forces, pressures and cavitation on 2-d sections suitable for marine current turbines. Proceedings of the Institution of Mechanical Engineers, Part M (Journal of Engineering for the Maritime Environment) 218, 127–38.

Moriarty, P.J., Hansen, A.C., 2005. AeroDyn theory manual. National Renewable Energy Laboratory, Salt Lake City, Utah, USA.

Murray, J., Barone, M., 2011. The development of cactus, a wind and marine turbine performance simulation code, in: 49th AIAA Aerospace Sciences Meeting including the New Horizons Forum and Aerospace Exposition. American Institute of Aeronautics and Astronautics. Aerospace Sciences Meetings.

Mycek, P., Gaurier, B., Germain, G., Pinon, G., Rivoalen, E., 2014. Experimental study of the turbulence intensity effects on marine current turbines behaviour. part i: One single turbine. Renewable Energy 66, 729–746.

Øye, S., 1991. Dynamic stall simulated as time lag of separation, in: Proceedings of the 4th IEA Symposium on the aerodynamics of wind turbines.

Rourke, F.O., Boyle, F., Reynolds, A., 2010. Marine current energy devices: Current status and possible future applications in ireland. Renewable and Sustainable Energy Reviews 14, 1026–1036.

Shulman, R., 2008. N.y. tests turbines to produce power URL: [online](September20,2008)http://www.washingtonpost.com/wp-dyn/content/article/2008/09/19/AR2008091903729.html[accessed25.10.2016].

Shyy, W., Lian, Y., Tang, J., Viieru, D., Liu, H., 2007. Aerodynamics of low Reynolds number flyers. volume 22. Cambridge University Press.

Tatum, S., Frost, C., Allmark, M., O'Doherty, D., Mason-Jones, A., Prickett, P., Grosvenor, R., Byrne, C., O'Doherty, T., 2016. Wave–current interaction effects on tidal stream turbine performance and loading characteristics. International Journal of Marine Energy 14, 161–179.

Whelan, J.I., 2010. A fluid dynamic study of free-surface proximity and inertia effects on tidal turbines. Ph.D. thesis. Imperial College London.

White, D., 2011. Editorial focus: tidal system challenge e blade design. Ocean News & Technology 17.

Zhang, L., Wang, S.q., Sheng, Q.h., Jing, F.m., Ma, Y., 2015. The effects of surge motion of the floating platform on hydrodynamics performance of horizontal-axis tidal current turbine. Renewable Energy 74, 796–802.

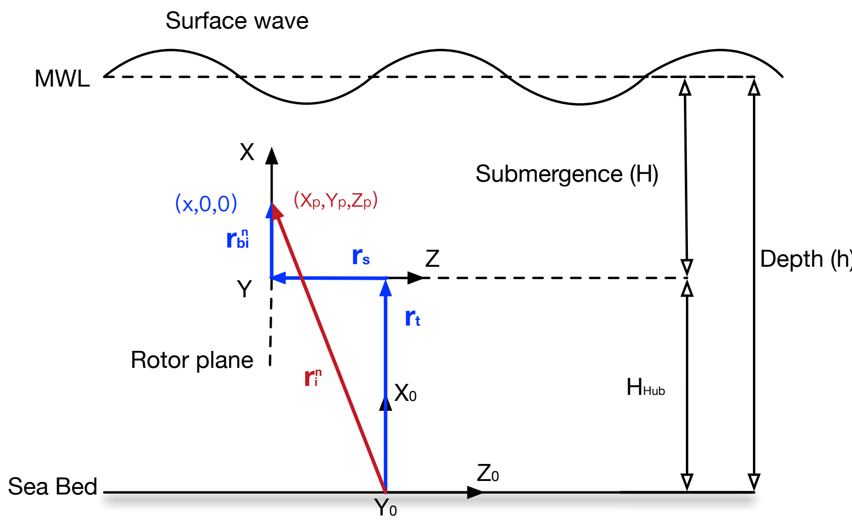

Figure 1: Position of blade element described in global coordinate.

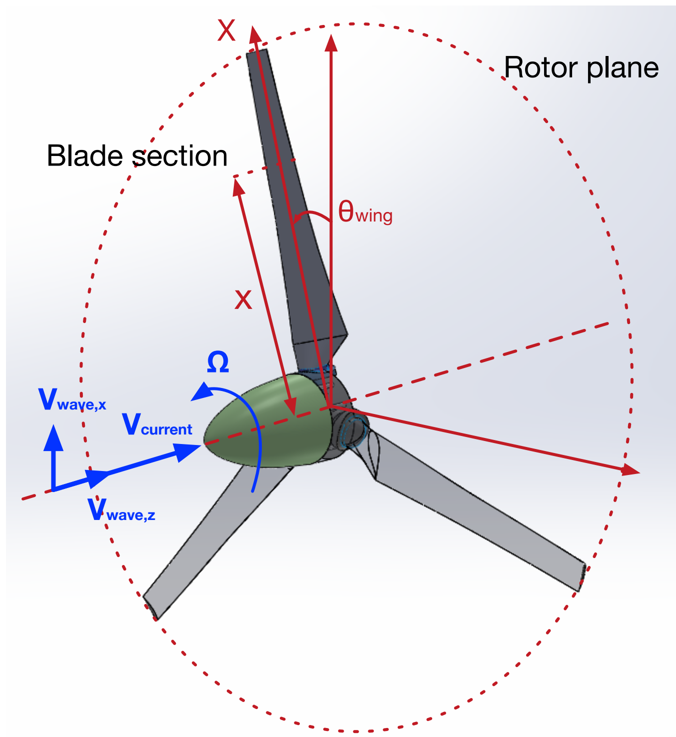

Figure 2: Azimuthal position of the blade element in rotor plane.

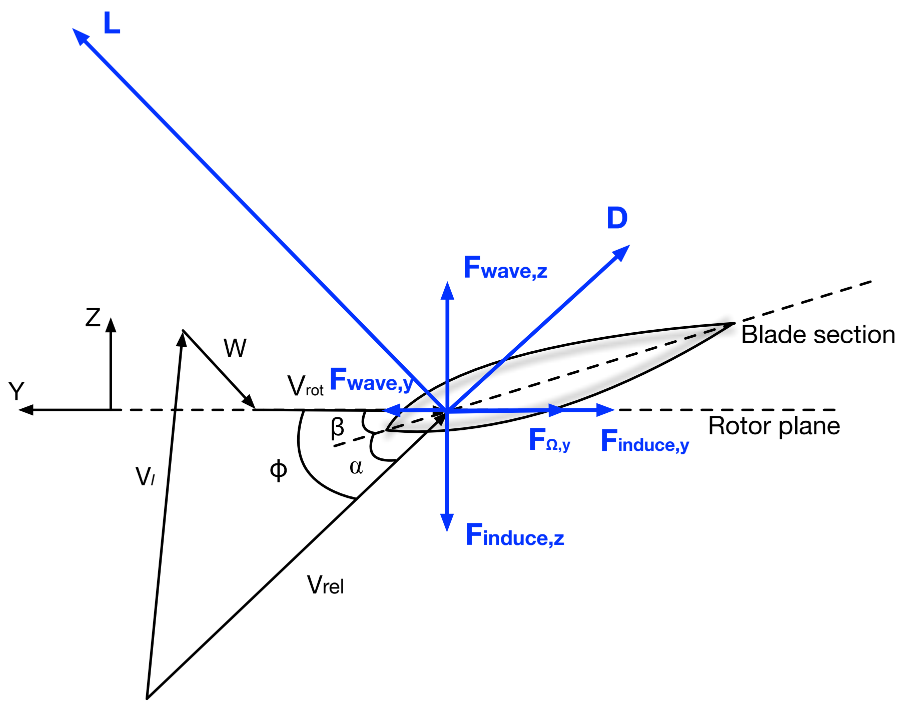

Figure 3: Velocity triangle and hydrodynamic forces acting on the blade section.

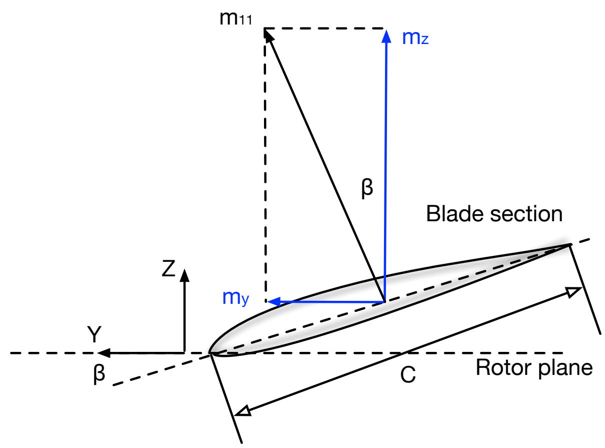

Figure 4: 2-D added mass in y and z direction of the blade section

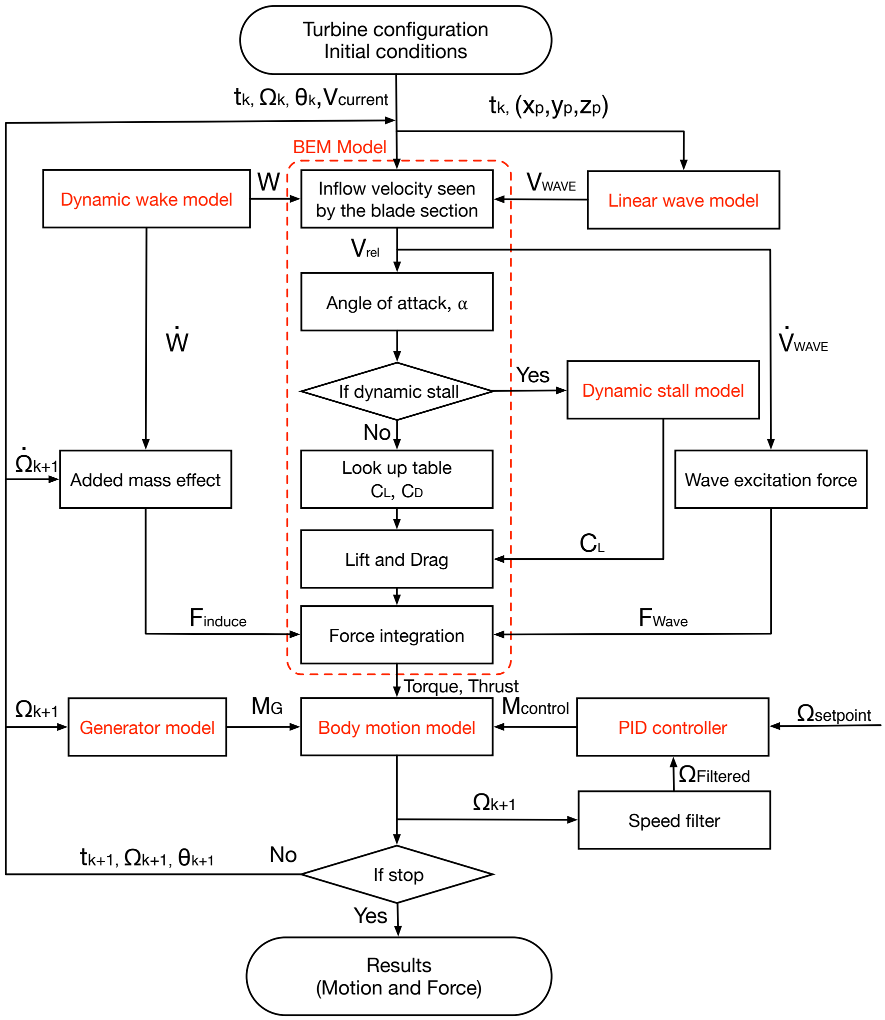

Figure 5: Flow chart of the numerical model with an inclusion of dynamic inflow model, dynamic stall model, linear waves, and added mass effects.

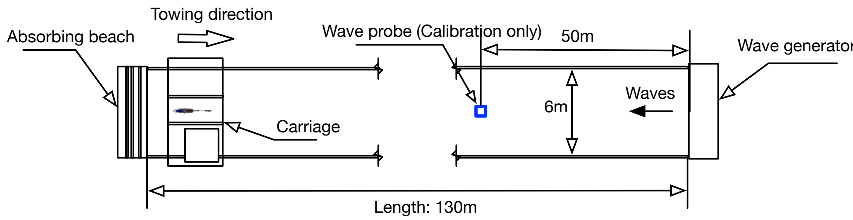

Figure 6: Schematic of the towing tank arrangement.

Figure 7: Photo of the 1:25 scaled turbine

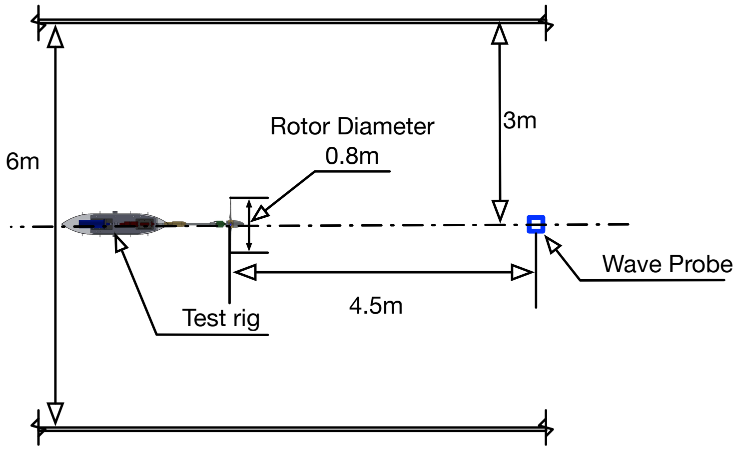

Figure 8: Schematic of the test rig and wave probe arrangement.

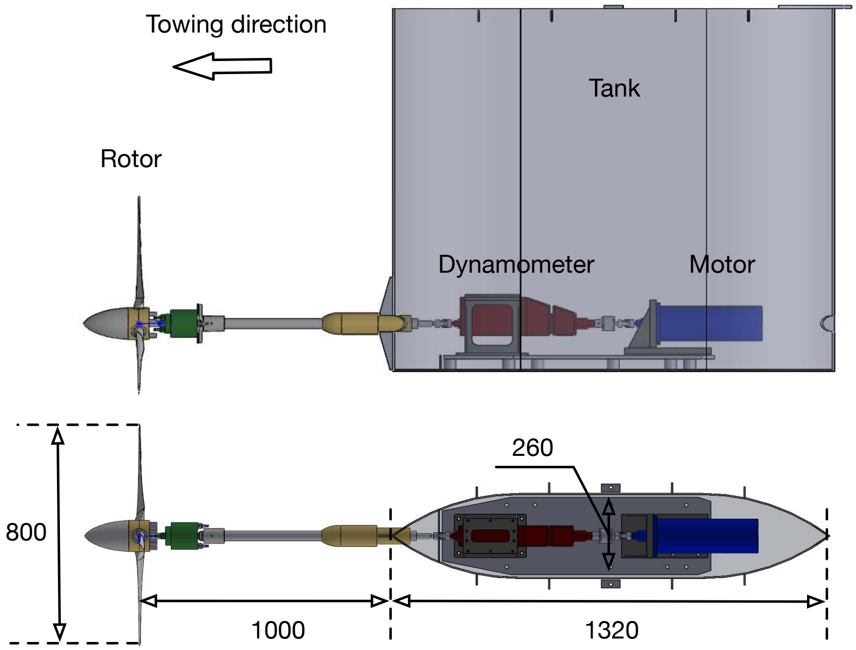

Figure 9: Test rig arrangement

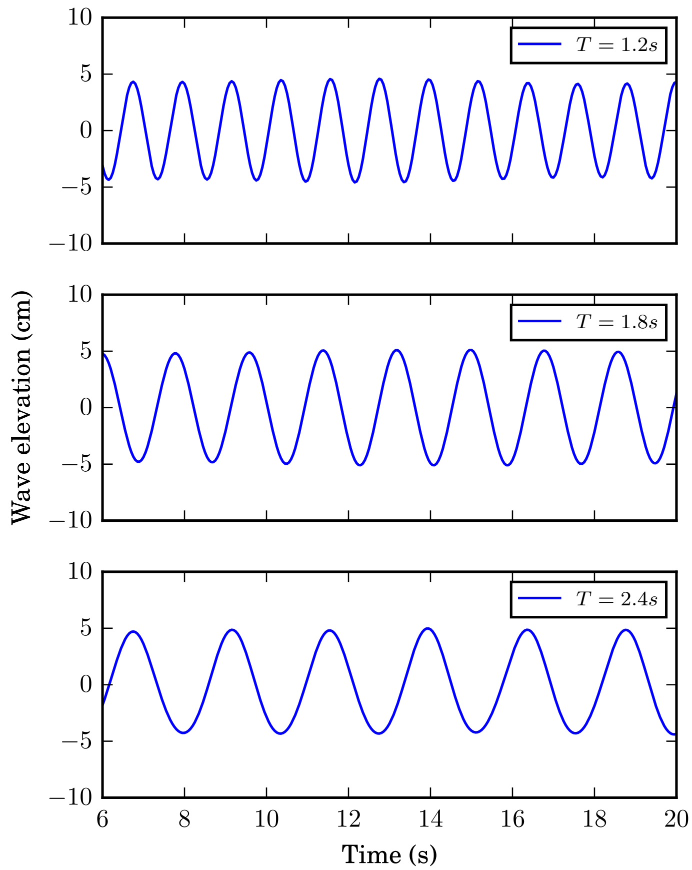

Figure 10: The selected time histories of the wave elevation with wave period of 1.2s, 1.8s, and 2.4s in calibration at model scale.

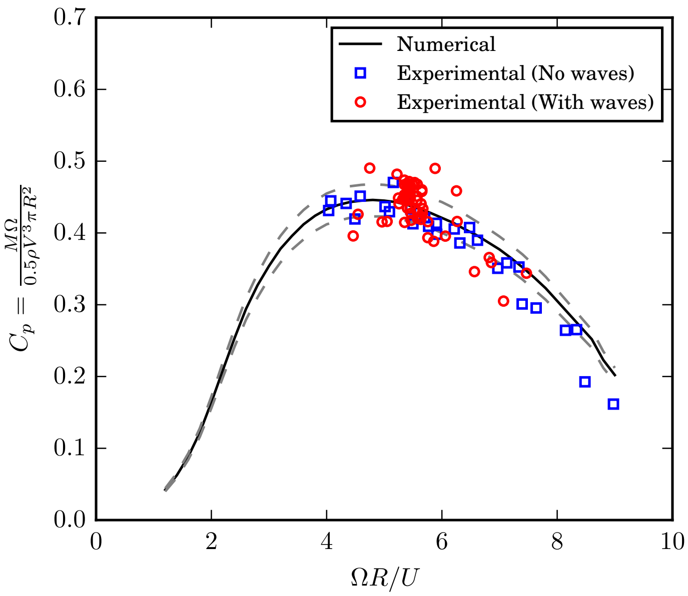

Figure 11: Power coefficient C_p as a function of TSR with and without the presence of waves, compared with the numerical prediction. The dash lines indicate ±5% errors.

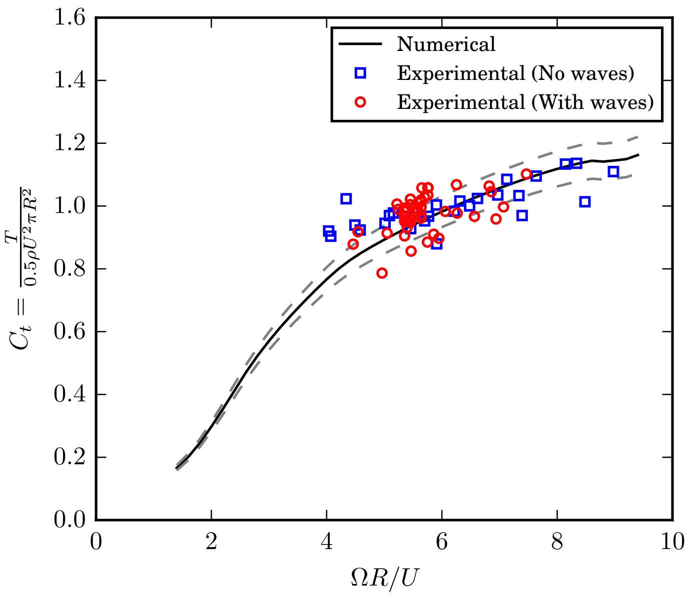

Figure 12: Thrust coefficient C_T as a function of TSR with and without the presence of waves, compared with the numerical prediction. The dash lines indicate ±5% errors.

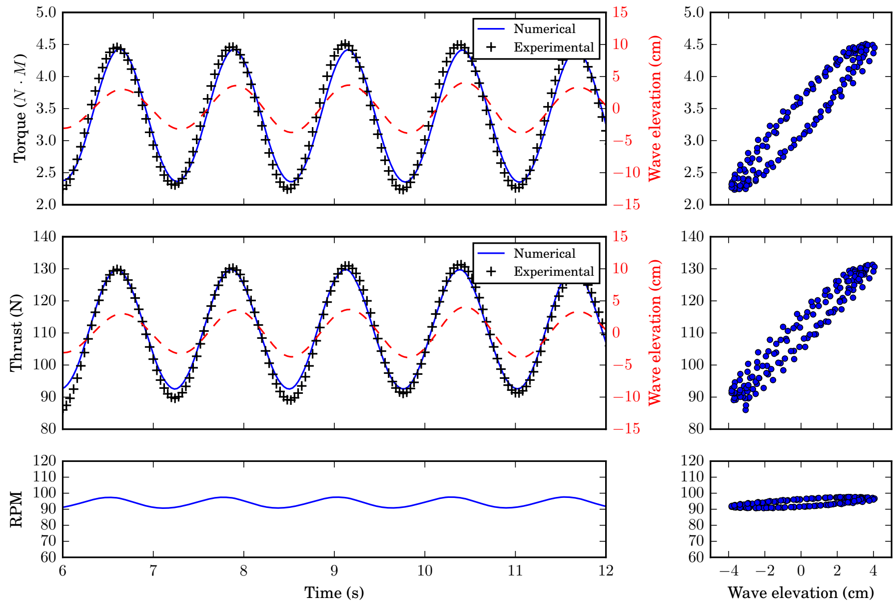

Figure 13: Time histories of the torque, thrust and rotational speed, and the torque, thrust and rotational speed as a function versus the encounter wave elevation, for $U = 0.68\,\mathrm{m\,s^{-1}}$, RPM = 94.2, $T_{wave} = 1.6\,\mathrm{s}$, $H_{wave} = 7\,\mathrm{cm}$, and submergence $H/D = 0.8$.

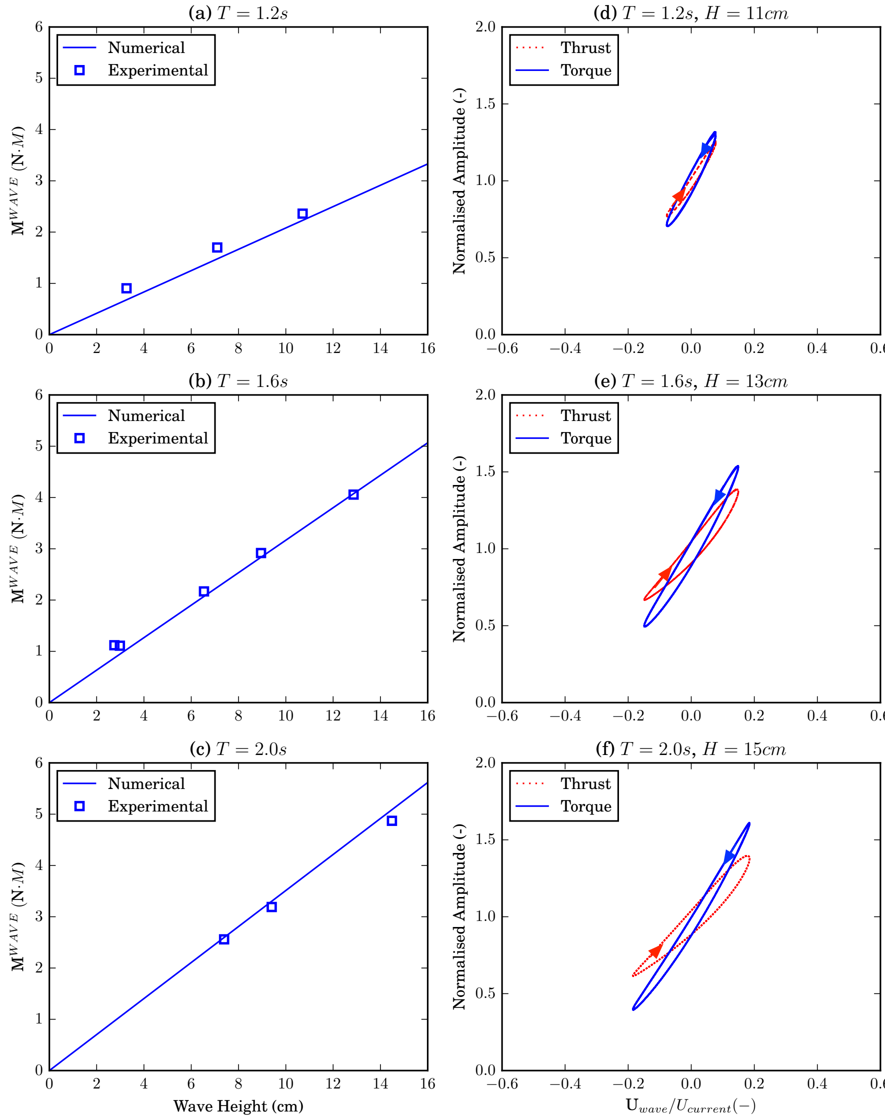

Figure 14: The range of the wave induced torque M^{wave} versus the wave height with different encounter wave periods (a, b, c), compared with the numerical prediction for $U = 0.68\,\mathrm{m\,s^{-1}}$, RPM = 87.6, and submergence $H/D = 0.8$. The amplitude of the thrust and torque normalized by the mean value respectively as a function of $U_{wave}/U_{current}$ (d, e, f).

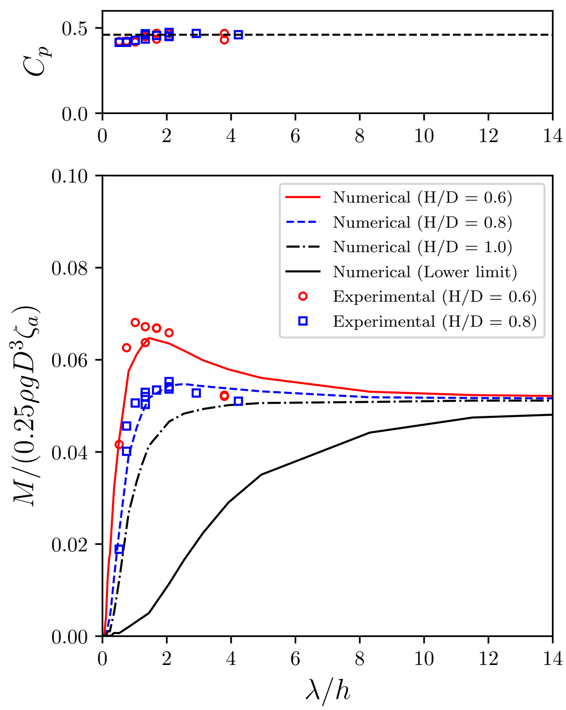

Figure 15: The range of the dynamic torque $M/(0.25\rho g D^3 \zeta_a)$ as a function of λ/h with difference submergence, compared with experimental data for $U = 0.68\,\mathrm{m\,s^{-1}}$, RPM = 87.6. The lower limit is restricted by the physical condition of water depth that the rotor hub is only 0.5D up on the sea bed. D is the diameter of the rotor, h is the water depth, and H is the submergence of the hub.

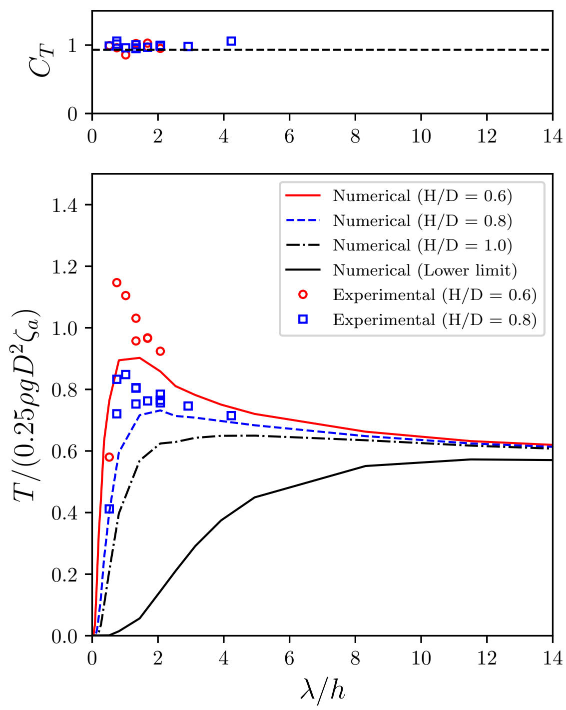

Figure 16: $T/(0.25\rho g D^2 \zeta_a)$ as a function of λ/h with difference submergence, for $U = 0.68\,\mathrm{m\,s^{-1}}$, RPM = 87.6. The lower limit is restricted by the physical condition of water depth that the rotor hub is only 0.5D up on the sea bed. D is the diameter of the rotor, h is the water depth, and H is the submergence of the hub.

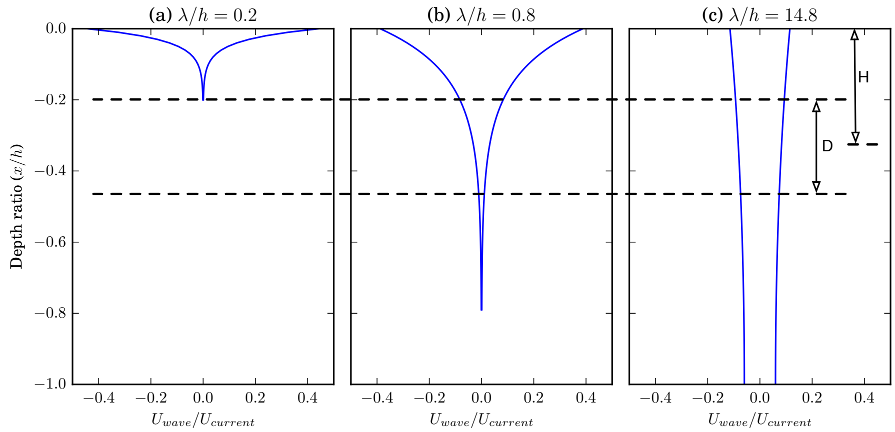

Figure 17: Horizontal wave particle velocity V_z^{Wave} profiles normalized by the undisturbed inflow velocity $U_{current} = 0.68\,\mathrm{m\,s^{-1}}$ with different λ/h. D is the rotor diameter and H is the submergence of the hub.

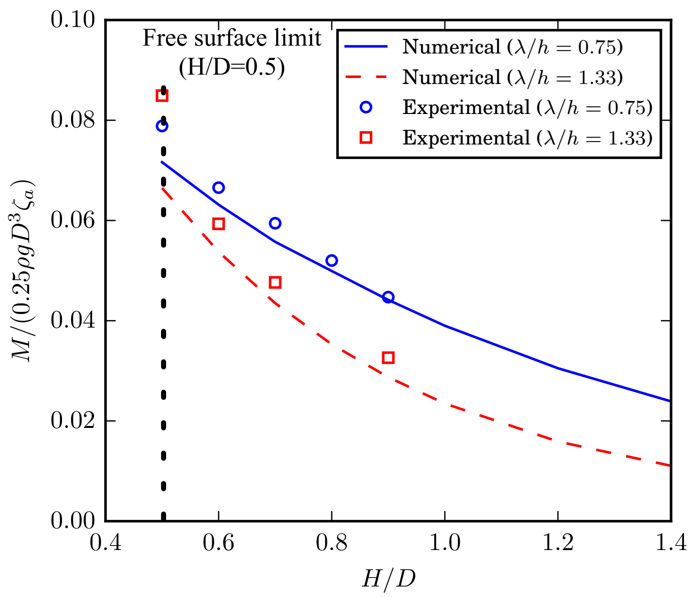

Figure 18: $M/(0.25\rho g D^3 \zeta_a)$ versus submergence H/D with λ/h = 0.75, 1.33, compared with the numerical predictions, for U = 0.68 m s^{-1}, RPM = 87.6 (TSR = 5.4).

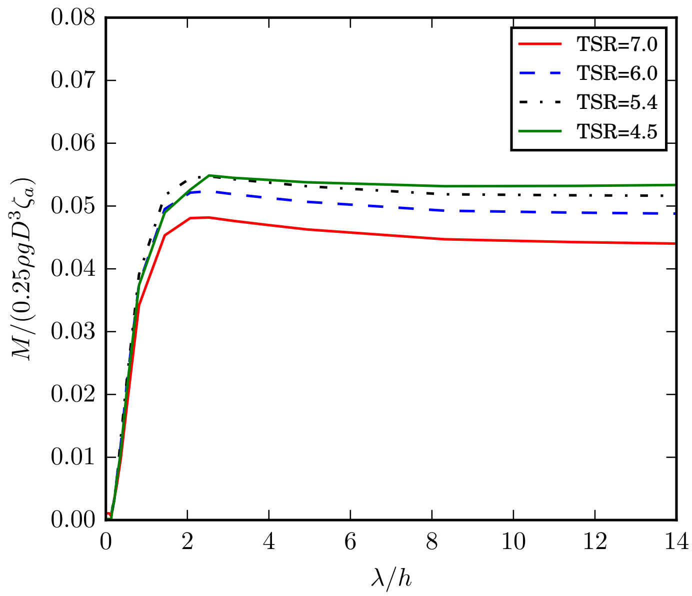

Figure 19: $M/(0.25\rho g D^3\zeta_a)$ as a function of λ/h with different tip speed ratios (TSR), for $U = 0.68\,\mathrm{m\,s^{-1}}$, submergence $H/D = 0.8$.

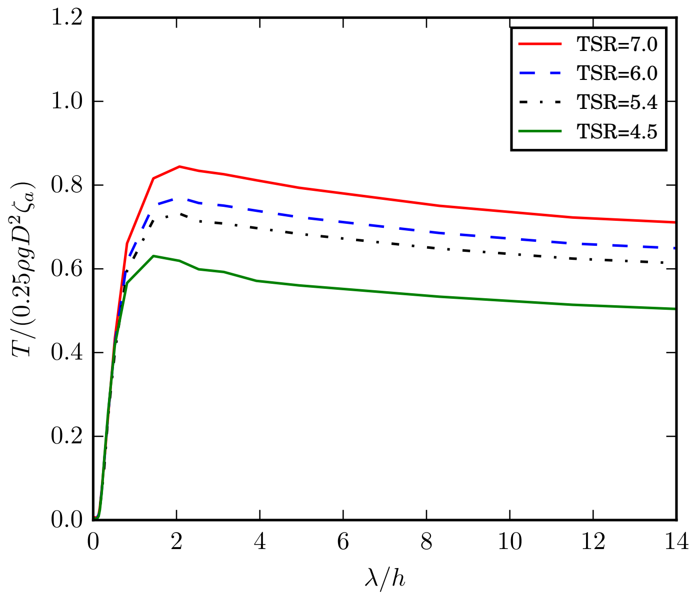

Figure 20: $T/(0.25\rho g D^2 \zeta_a)$ as a function of λ/h with different tip speed ratios (TSR), for $U = 0.68\,\mathrm{m\,s^{-1}}$, submergence ratio $H/D = 0.8$.

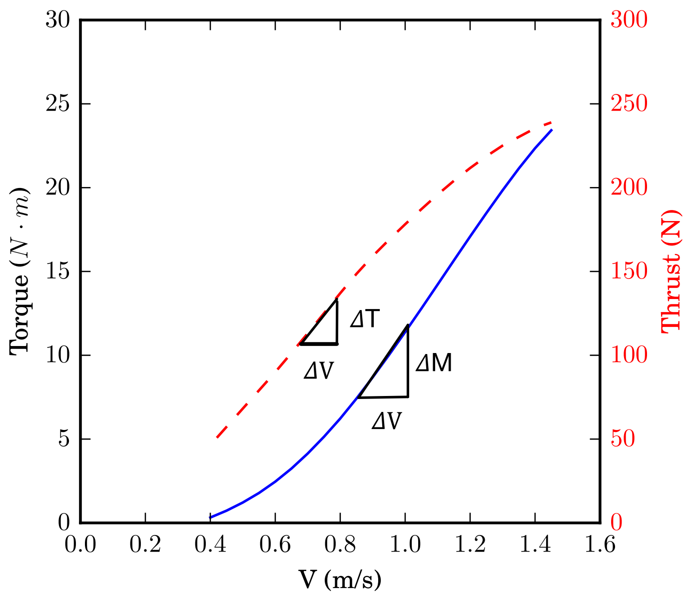

Figure 21: Torque and thrust as a function of the inflow velocity U at constant rotational speed RPM = 87.6.

Table 1: Particulars of the tidal turbine blades at model scale.

r/R	r (mm)	Pre-Twist (deg)	Chord (mm)	t/c (%)
0.125	50	20.0	32.0	99.9
0.200	80	19.5	67.9	22.0
0.300	120	16.5	60.7	20.0
0.400	160	13.3	51.9	18.3
0.500	200	11.6	47.6	14.8
0.600	240	9.4	43.3	14.2
0.700	280	7.3	40.1	13.6
0.800	320	5.2	37.6	13.1
0.900	360	2.7	35.3	12.5
1.000	400	0.0	33.2	12.0

Table 2: Regular wave parameters used for wave calibration. (Model scale)

period (s) T	height (cm) H	Length (m) λ	steepness (%) $\gamma = H/\lambda$	Length depth ratio (-) λ/h
1.0	5.0	1.56	3.21	0.520
1.2	5.0	2.25	2.22	0.749
1.4	8.0	3.06	2.61	1.020
1.6	8.0	4.00	2.00	1.332
1.6	5.0	4.00	1.25	1.332
1.6	8.0	4.00	2.00	1.332
1.6	12.0	4.00	3.00	1.332
1.8	8.0	5.06	1.58	1.686
2.0	8.0	6.22	1.29	2.072
2.4	10.0	8.75	1.14	2.918
2.8	10.0	11.38	0.88	3.793
3.0	10.0	12.68	0.79	4.228

Table 3: Reduced frequency k and current number μ of the typical cases with different waves and towing conditions. The towing velocity was fixed at $0.68\,\mathrm{m\,s^{-1}}$.

Case No.	Waves		Towing condition		Reduced frequency	Current number
	T (s)	H (cm)	Submergence (m)	TSR (-)	$k = \pi f c/V$	$\mu = \tilde{u}/U$
1	1.0	5	0.64	5.4	0.044	0.018
2	1.2	8	0.64	5.4	0.037	0.052
3	1.6	10	0.64	5.4	0.028	0.106
4	2.4	10	0.64	5.4	0.018	0.127
5	3.0	10	0.64	5.4	0.015	0.130
6	1.2	8	0.64	4.5	0.044	0.052
7	1.2	8	0.64	6.0	0.033	0.052
8	1.2	8	0.64	7.0	0.028	0.052
9	1.6	10	0.36	5.4	0.028	0.164
10	1.6	10	0.56	5.4	0.028	0.120
11	1.6	10	0.72	5.4	0.028	0.093

Table 4: Estimation of the k_M^{ST} and k_T^{ST} with different tip speed ratios by the long wave approximation and by the quasi-static method, at inflow velocity $U = 0.68\,\mathrm{m\,s^{-1}}$.

		Long wave approx.		Quasi-static method	
Case No.	TSR	k_M^{ST} (Fig. 19)	k_T^{ST} (Fig. 20)	k_M^{ST} (Eqn. 49)	k_T^{ST} (Eqn. 50)
1	4.5	0.054	0.421	0.056	0.429
2	5.4	0.051	0.522	0.052	0.535
3	6.0	0.048	0.555	0.048	0.576
4	7.0	0.043	0.613	0.043	0.643